ARTICLE

Room Temperature Aerosol Dehydration of Green Fluorescence Protein

Zehao Pan[a], Junshi Wang[a], Howard A. Stone[a], and Maksim Mezhericher[a,b]

[a]Department of Mechanical and Aerospace Engineering, Princeton University, Princeton, New Jersey 08544, USA
[b]INAEDIS, INC., Princeton, New Jersey 08540, USA

ARTICLE HISTORY
Compiled September 17, 2024

ABSTRACT
Rapid Room-Temperature Aerosol Dehydration (RTAD) is a new, scalable drying technology for pharmaceutical drug products. Compared to conventional spray drying, RTAD uses sub-20 μm droplets that quickly evaporate at ambient temperature, which reduce drying-induced stress for thermally sensitive biologics. In this work, we used green fluorescence protein (GFP) as a model biological molecule to optimize the RTAD system design. We studied the effects of polysorbate 20 (a model surfactant), droplet size, and the flow pattern in the drying chamber on GFP fluorescence after drying and powder reconstitution. We found that the presence of polysorbate 20 in the formulation has a significant impact on the GFP fluorescence, especially for smaller droplets. GFP fluorescence is also affected by the flow pattern in the drying chamber as revealed by Computational Fluid Dynamics (CFD) simulations. We found that non-axisymmetric flow patterns and closed circulating streamlines near the drying gas inlet can negatively affect the GFP fluorescence. The work reported here demonstrates GFP as a sensitive biologic for assessing bioactivity following dehydration processing, which can be used for efficient development novel RTAD drying process.

KEYWORDS
Room-temperature aerosol dehydration; Biologic drying; Particle engineering; Green Fluorescence Protein; Computational Fluid Dynamics.

1. Introduction

Dehydration of biological pharmaceutical products is a critical step in drug product manufacturing for dry powder inhalation, intranasal drug delivery, and vaccine stabilization. Due to the sensitivity of many protein biopharmaceuticals to temperature, we leveraged our prior fundamental studies on aerosol generation (*1*, *2*) and developed a method for laboratory-scale Rapid Room-Temperature Aerosol Dehydration (RTAD). Compared to spray drying, RTAD leverages much smaller droplet size (sub-20 μm) to enhance the rate of solvent evaporation rather than relying on elevated temperature of the drying gas. In our recent study, we demonstrated RTAD offers a system for room-temperature dehydration of liquid biopharmaceutical formulations of antigen-binding fragment (Fab) of monoclonal antibody with reduced product degradation compared

CONTACT Maksim Mezhericher. Email: maksymm@princeton.edu

to traditional spray drying (*3*).

Despite the reduction of thermal stress from the use of RTAD, biological products could still be subject to interfacial and shear stresses during the atomization and drying steps in RTAD (*4*). In this work, we used Green Fluorescent Protein (GFP) as a model biological molecule to assess the efficacy of our approach for retaining biological activity and to optimize the RTAD formulation, including the conditions of the drying gas. If GFP experiences a structural variation during the process, such as unfolding or aggregation, the excitation and emission spectrum of GFP would be altered, resulting in shifts in fluorescence intensity at a fixed wavelength of the measurement (*5–7*). Thus, by comparing the fluorescence intensity of GFP at fixed wavelength before and after dehydration, we can assess the effect of the external stresses induced by drying of GFP.

Through this approach, we identified three major conditions in RTAD that can affect the GFP fluorescence intensity, including the use of surfactant, droplet size, and the drying gas recirculation patterns in the RTAD chamber. The work demonstrated that GFP can be used as a model biological molecule to test the design of the feedstock formulation, feedstock atomization, and chamber flow patterns of RTAD and, in general, other spray drying systems.

2. Methods and Materials

2.1. *Materials*

Mannitol and polysorbate 20 were purchased from Sigma Aldrich (USA). 1X Tris-EDTA buffer (pH 7.4), which contains 10 mM tris(hydroxymethyl)aminomethane and 1 mM ethylenediaminetetraacetic acid, was purchased from Fischer Scientific (USA). Technical grade GFP was purchased from Protein Mods (Wisconsin, USA). The PVDF filters were purchased from Tisch Scientific (Ohio, USA). In all feedstock formulations, 1X Tris-EDTA buffer, 7.5 wt% mannitol, and 0.03 mg/ml GFP were used. When surfactant was present, 0.4 mg/ml polysorbate 20 was added to the feedstock.

2.2. *Droplet size distribution*

The droplet size distribution of the atomizer was measured with laser diffractometry (Spraytec, Malvern Panalytical, UK). We used water to build a calibration curve of the median droplet size distribution (Dv50) and D_{32} (Sauter mean diameter) as a function of the atomizing pressure at a constant feed liquid flow rate, as shown in Figure 1. Dv50 represents the diameter at which 50% of the total volume of the aerosol is in droplets with diameter smaller than Dv50. D_{32} reflects the surface-area-to-volume ratio of the aerosol, which is the same as a sphere with the diameter D_{32}. Our measurements show that across all atomization pressures used in the study, where the liquid flow rate varies by a factor of 25 from minimum to maximum, the droplet volume varies less than a factor of 3 in terms of either Dv50 or D_{32}.

For solutions with 0.4 mg/ml of polysorbate 20, the surface tension is reduced to 37 mN/m (*8*), about half that of water. In an atomization regime with a low viscosity solution, where the viscous forces are much smaller than the inertial and surface tension forces, the droplet diameter is proportional to the surface tension (*9*). This feature allows us to calculate the atomizing drop Dv50 for polysorbate 20 solution based on the calibration curve for water.

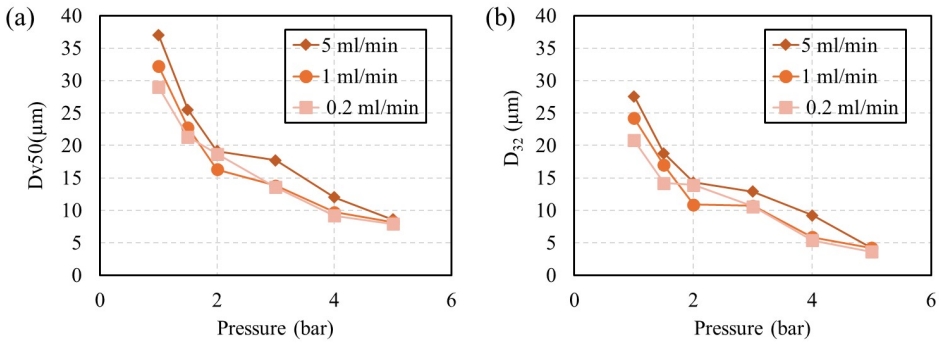

Figure 1. (a) Dv50 and and (b) D_{32} (Sauter mean diameter) of the atomizer used in this study as a function of atomizing pressure at different liquid feed flow rates.

2.3. *Characterization of the change in GFP fluorescence after drying*

After a typical experiment, the excitation and emission spectra of the reconstituted powder were measured and compared with those of the unprocessed feedstock solution. Typical data is shown in Figure 2(a). The excitation spectra were measured by scanning excitation wavelengths while fixing emission at 525 nm. The emission spectra were measured by scanning emission wavelengths while fixing excitation at 450 nm. The GFP has an absorption peak at 475 nm and emission peak at 505 nm for both reconstituted and feedstock solutions.

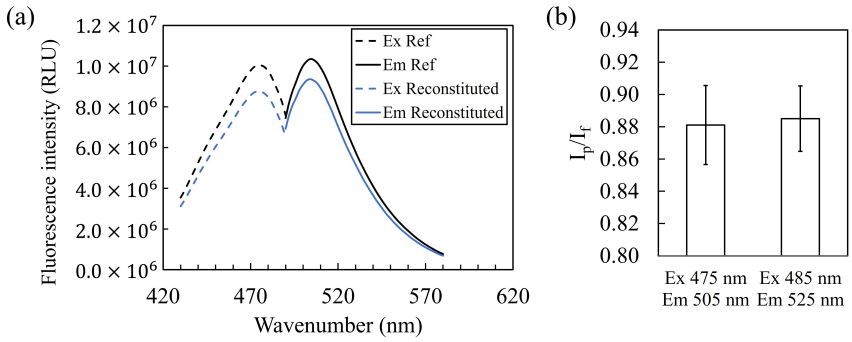

Figure 2. (a) Excitation and emission spectra of GFP before and after drying. The dashed lines are excitation spectra; the solid lines are emission spectra. The excitation spectra were measured by scanning excitation wavelengths while fixing emission at 525 nm. The emission spectra were measured by scanning emission wavelengths while fixing excitation at 450 nm. (b) The ratio of GFP fluorescence after and before drying measured at Ex 475 nm - Em 505 nm and Ex 485 nm - Em 525 nm.

To measure the fluorescence intensity of GFP after drying, the powder was weighed and reconstituted with DI water to the same concentration as the feedstock solution used in the RTAD, i.e. 0.03 mg/ml GFP. Either the feedstock or the reconstituted powder was pipetted into five wells of a half-area 96-well plate (Corning, NY, USA), with each well receiving 100 μl. The fluorescence intensities of the feedstock (I_{f}) or the reconstituted powder (I_{p}) were measured using a plate reader (SpectraMax i3x, Molecular Devices, San Jose, CA). The fluorescence ratio $I_{\mathrm{f}}/I_{\mathrm{p}}$ was calculated, with error bar calculated as the standard deviation of the ratio of two random variables I_{f}

and I_p, defined as (*10*)

$$\sigma\left(\frac{I_\mathrm{f}}{I_\mathrm{p}}\right) = \frac{\mu_{I_\mathrm{f}}}{\mu_{I_\mathrm{p}}}\left[\frac{\sigma^2_{I_\mathrm{f}}}{\mu^2_{I_\mathrm{f}}} - 2\frac{\mathrm{cov}(\mathrm{I_f}, \mathrm{I_p})}{\mu_{I_\mathrm{f}}\mu_{I_\mathrm{p}}} + \frac{\sigma^2_{I_\mathrm{p}}}{\mu^2_{I_\mathrm{p}}}\right]^{1/2}, \tag{1}$$

where μ_{I_f} and μ_{I_p} are the means, σ_{I_f} and σ_{I_p} are the standard deviations, and $\mathrm{cov}(I_\mathrm{f}, I_\mathrm{p})$ is the covariance of I_f and I_p.

Two pairs of excitation (Ex) and emission (Em) wavelengths were used: 1) Ex 475 nm - Em 505 nm; 2) Ex 485 nm - Em 525 nm, as shown in Figure 2(b). The two options show similar $I_\mathrm{p}/I_\mathrm{f}$, but the latter has a slightly tighter confidence level. Thus, we used Ex 485 nm - Em 525 nm to quantify the variation of fluorescence intensity after drying for all RTAD runs.

2.4. *Drying chamber design and operating parameters*

The drying chamber is a cylinder made of stainless steel having 247 mm in inner diameter and 610 mm in length. The drying gas inlet and atomization nozzle reside in the top cover of the chamber. The drying gas was nitrogen. The flow rate of the drying gas was 50 SLPM (L/min at standard conditions for pressure (1 bar) and temperature (0°C)), while the flow rate of the atomizing gas through the atomization nozzle was 10 SLPM. The flow rate of the liquid to be atomized was 0.5 ml/min.

The Reynolds number ($\mathrm{Re} = uD/\nu$) of the drying gas and the atomizing gas are 9000 and 10500, respectively, where u is the gas velocity at the inlet/nozzle, D is the diameter of the gas inlet/nozzle, and ν is the kinematic viscosity of nitrogen at 22°C.

The bottom of the drying chamber uses a 0.45 μm polyvinylidene fluoride (PVDF) filter on a filter plate for collection of dried particles. For each RTAD experiment, a batch of 10 ml solution was prepared, where 8 ml was used as feedstock to be dehydrated and 2 ml was saved as a reference.

Three configurations with different drying gas inlet designs were constructed and studied, as shown in Figure 3. The drying gas flow rate and the liquid feedstock rate were fixed at 50 SLPM and 0.5 ml/min. The flow rate of the liquid feedstock is limited by the drying gas flow rate supplied by the drying gas system to ensure a dried product.

In configuration A, the drying gas was injected from a port placed 100 mm away from the center of the top plate, where the drying gas inlet velocity was 6.6 m/s. In configuration B, the drying gas was introduced from the center into a cylindrical plenum chamber. Compared to configuration B, configuration C has a diffuser in the plenum. The inlet gas velocity was 24.9 m/s for both configurations B and C.

The studied experimental conditions are summarized in Table 1. Different droplet sizes are varied by choosing the atomization pressure and changing the surface tension with polysorbate 20. Three drying gas inlet configurations are tested with the same feedstock formulation and droplet sizes in runs labeled 4, 5 and 6.

2.5. *Computational Fluid Dynamics Modeling*

We conducted three-dimensional, full-scale, steady-state Computational Fluid Dynamics (CFD) modeling and numerical simulations of the RTAD processes in chambers with three designs of the drying gas inlet (see Figure 3), including Configuration A:

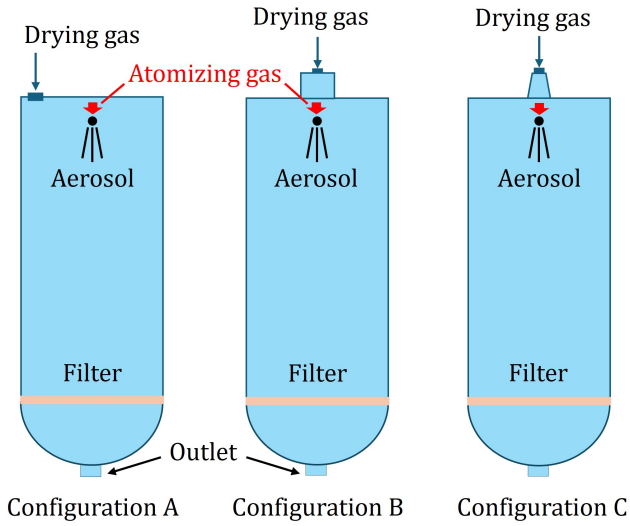

Figure 3. Schematic of drying chamber configurations used in the study of laboratory-scale RTAD process. Configuration A has a drying gas inlet 100 mm away from the center, while Configurations B and C have gas inlets in the center. A diffuser is added at the inlet for Configuration C. All three chambers have an atomization nozzle placed in the center with atomization gas flowing through to generate droplets. Drying particles are collected at the filter.

Table 1. Experimental conditions of all runs of RTAD. Dv50 is calculated based on the atomization pressure using the relationship in Figure 1 and accounting for presence of absence of surfactant polysorbate 20. The feedstock solution for all runs contained 0.03 mg/ml GFP, 75 mg/ml mannitol and 1X Tris-EDTA buffer.

Run	Dv50 (μm)	Polysorbate 20 (mg/ml)	Configuration
1	11.2	0	A
2	21.1	0	A
3	24.7	0	A
4	7.5	0.4	A
5	7.5	0.4	B
6	7.5	0.4	C
7	12.4	0.4	C
8	14.2	0.4	C
9	16.6	0.4	C

side port inlet, Configuration B: center port inlet without diffuser, and Configuration C: center port inlet with diffuser. The simulations were performed using the ANSYS Fluent 2024 R1 CFD software package. In this study, we utilized previously developed CFD model of spray drying process by Mezhericher et al. (*11*, *12*) as a staring point.

The multiphase flow in the drying chamber was considered by using Eulerian-Lagrangian Discrete Phase model (DPM). The gas was considered as a continuous phase (Eulerian approach), and droplets and particles as discrete phase (Lagrangian approach). The governing equations for gas phase included the Reynolds-Averaged Navier-Stokes (RANS) equations and the energy equation, with gravity considered. In addition, the gas was considered to be ideal, and the respective constitutive equation of ideal gas was utilized. The realizable k-ϵ turbulence model with standard wall functions was employed for viscous modeling. Species transport was considered for a nitrogen and water vapor mixture, treated as an ideal gas. The evaporation and dynamics of the droplets were modeled using multi-component, cone-shape injections at the nozzle exit (Figure 4a). We described the hollow spray cone by 500 DPM droplet

injections and employed the Rosin-Rammler distribution to simulate the size distribution of droplets in spray. For that purpose, each DPM droplet injection was modeled by 25 different diameters, ranging from 0.5 µm to 30 µm at 22°C. The droplet size distribution was identical to the droplet distribution measured by laser diffraction at 2 bar and 1 ml/min, as shown in Figure 1. As the droplets traveled through the chamber, carried by the streams of drying and atomizing gas mixing together, they were either collected by the filter or trapped on the chamber walls.

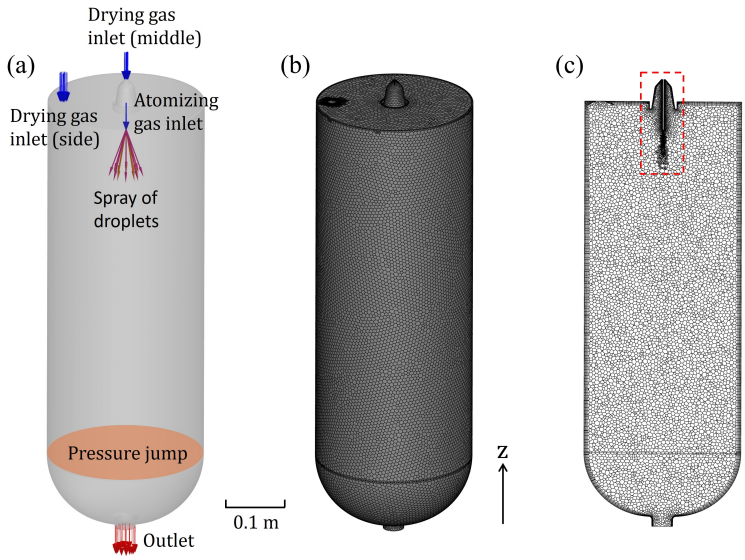

Figure 4. Computational modeling of RTAD process in laboratory-scale drying chamber. (a) Drying chamber geometry with boundary conditions including drying gas inlets at the center and side, atomizing gas inlet and cone-shape droplet injections from the spray nozzle, pressure jump on the particle filter, and gas outlet of the chamber. (b) Polyhedral numerical mesh at the internal chamber surface. (c) Polyhedral numerical mesh on the middle vertical cross section plane of the computational domain. The numerical mesh was refined by using the Adaptive mesh refinement (AMR) algorithm applied to the mesh cells where the gradient of the gas velocity magnitude was higher than 15% of the global maximum of the gas velocity gradient.

For the boundary conditions, mass flow inlets were applied for both the drying gas and atomizing gas (Figure 4a). The drying gas was introduced from a side port for configuration A and the center port for configurations B and C (Figure 3). The atomizing gas was injected at the nozzle exit in all configurations. Both the drying gas and atomizing gas at the inlet to the domain were set to be pure nitrogen at 22°C with flow rates of 50 SLPM and 10 SLPM, respectively. A pressure jump boundary condition was applied at the filter where dried particles were collected, and a pressure outlet was specified at the chamber exit (Figure 4a). The chamber wall was modeled as a no-slip surface. The ambient room temperature was also set to 22°C for modeling the convective thermal boundary condition at the chamber wall, made of stainless steel. To simulate droplet drying kinetics, all the injected droplets were considered as a mixture of two components, evaporating water and non-evaporating solid material. For simplicity, both droplet components were assumed to have density, thermal conductivity, and heat capacity of water. Once the evaporating component of the droplet was fully vaporized, which was considered once the water content in the droplet decreased below 5 wt%, the droplet was assumed to be a non-evaporating spherical particle on the next calculation steps.

A polyhedral mesh was used for the computational domain (Figure 4b), with adaptive mesh refinement (AMR) in regions exhibiting a high gradient of velocity mag-

nitude (Figure 4c). A mesh size study was performed to ensure numerical stability, solution accuracy, and independence of the mesh cell size. More details on the computational setup and on the mesh-independence studies can be found in the Appendices A and B.

2.6. *Single droplet drying regime*

Single droplet evaporation times from different simulation runs can be calculated using the drying kinetic model we previous developed (*11–13*). The model calculates the equilibrium evaporation period during the first drying stage before the initial crust forms over the droplet surface.

For experiments listed in Table 1, the droplet evaporation time is calculated in a scenario where the relative humidity (RH(%)) of the surrounding gas is 5% and the gas velocity relative to the droplet is 1 m/s, as shown in Figure 5(a). The Dv50 of each run are plotted as points on the graph.

The reduced droplet temperature due to evaporative drying can be calculated using the same drying kinetic model. Depending on RH of the surrounding gas, the droplet is cooled at different degrees. Typical results from the drying kinetic model when the surrounding gas has 5% and 30% RH are shown as lines in Figure 5(b). In all RTAD experiments listed in Table 1, the RH in the chamber is typically controlled between 5% and 30% during operation.

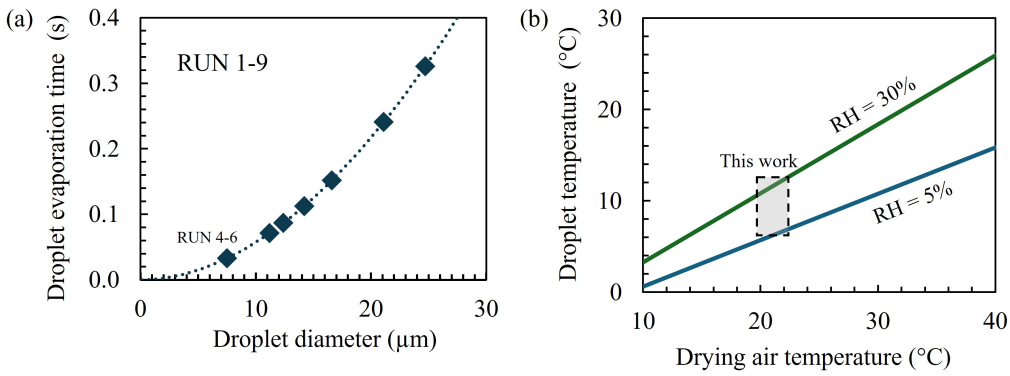

Figure 5. Single droplet drying regime for experiments in Table 1. (a) Droplet evaporation time as a function of droplet size. Line is calculated based on Equation 20 in (*12*) using relative humidity (RH(%)) of 5% and gas velocity relative to the droplet at 1 m/s. Data points are specific Dv50 values used in Table 1. (b) Droplet temperature due to evaporative drying. Lines are theoretical curves based on the wet bulb temperature at fixed RH. Shaded square indicates operating regime.

3. Results

3.1. I_p/I_f *as a function of drying gas inlet configuration*

The gas flow patterns across the drying chamber and near the drying gas inlet are shown in the "Drying gas inlet" panels in Figure 6. Compared to configurations B and C, the aerosol produced in configuration A is released outside of the center of the drying gas flow as it enters the chamber. In configuration B, strong recirculation zones appear at the corner of the cylindrical plenum housing the drying gas inlet. In

configuration C, the recirculation zone in B disappeared after replacing the cylindrical plenum with a conical diffuser, which has a divergence angle of 8° (*14*).

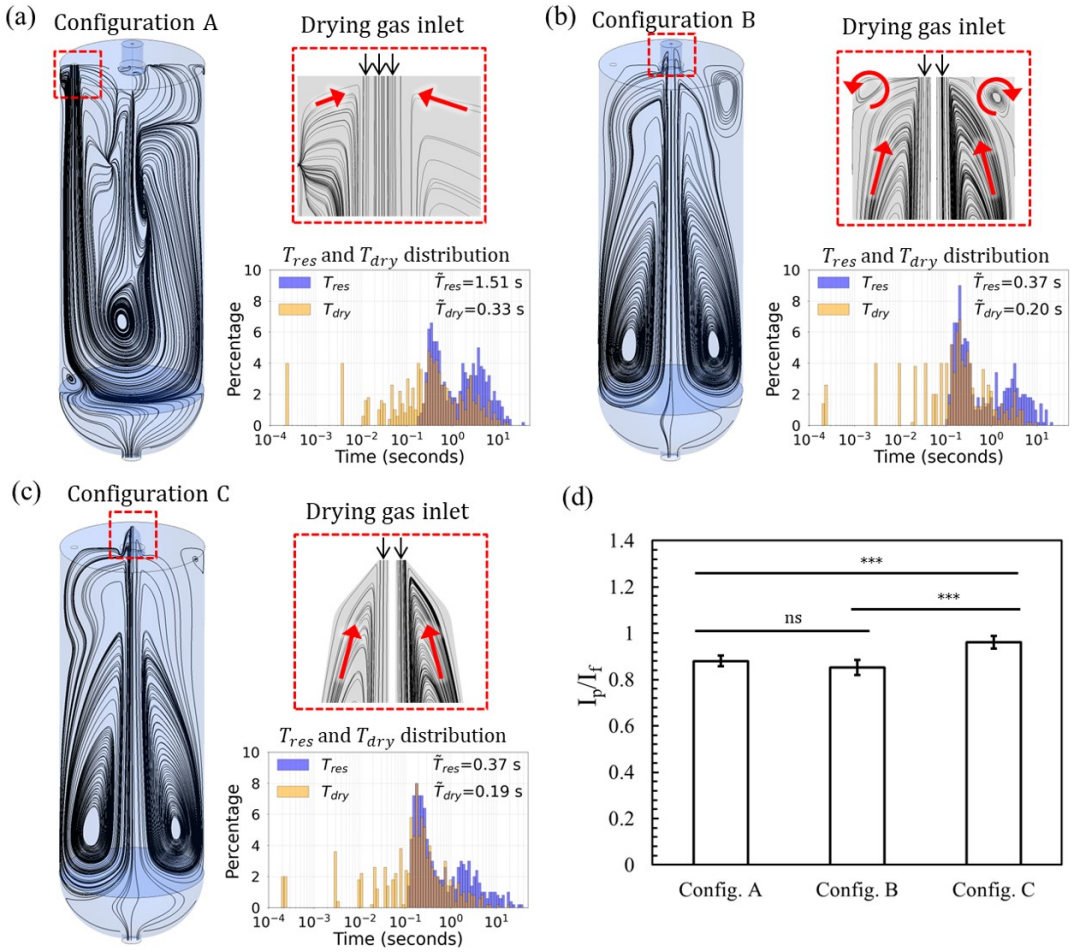

Figure 6. (a-c) CFD simulation of the RTAD process for drying chamber configuration A (a), B (b) and C (c). For each configuration, the panels display gas streamlines for the entire chamber, along with an enlarged view near the drying gas inlet, highlighted by a red square. Additionally, the residence time T_{res} and drying time T_{dry} distributions for each simulation are plotted. (d) Experimental results of I_p/I_f of GFP processed with chamber configurations A, B and C. ns: not significant; $***: p < 0.001$ (Student's t-test assuming same I_p/I_f between two configurations).

The history of a single droplet drying during RTAD is analyzed by two characteristic times: particle residence time (T_{res}), defined as the duration during which a drying droplet or dried particle remains airborne, and the droplet drying time (T_{dry}), defined as the period during which a droplet retains water content larger than final residual water content set to 5 wt% in this study.

The distributions of T_{res} and T_{dry} are plotted in the "T_{res} and T_{dry} distribution" panels in Figure 6. Under uniform drying conditions, T_{dry} is monotonically related to droplet diameter according to the single droplet drying kinetics model (Figure 5(a)). Since a unimodal droplet size distribution is assumed for the droplets sprayed by the RTAD atomizer, uniform drying conditions in RTAD chamber are expected to result in a unimodal T_{dry} distribution for dehydrated droplets. The near unimodal T_{dry} distribution observed in configuration C indicates a near uniform drying condition for all the droplets compared to the other two configurations. The longer median

$\tilde{T}_{dry} \approx 0.3$ s for configuration A compared to $\tilde{T}_{dry} \approx 0.2$ s for configuration B and C, reflects the effect of the chamber design in configuration A with off-center drying gas inlet and centerline-located liquid atomizer promotes larger recirculation zone with longer drying times.

The CFD numerical simulations predicted that the median $\tilde{T}_{res}$ is approximately 1.5 s for configuration A, and 0.4 s for configuration B and C. The longer time the droplets/particles stay airborne in the gas flow suggests that dried particles could re-enter the region near the atomizer multiple times and be repeatedly subjected to high gradients of velocity, humidity, temperature, pressure, and species. In addition, there are higher chances of inter-particle or particle-wall collisions before particles will be captured by the filter.

The effect of the flow pattern on the fluorescence intensity of dehydrated GFP was tested with experiments using the three drying chamber designs. The $I_{\mathrm{p}}/I_{\mathrm{f}}$ from run 4, 5 and 6 are shown in Figure 6 (d). The difference between $I_{\mathrm{p}}/I_{\mathrm{f}}$ from configuration C and configuration A/B are statistically significant (p-values from Student's t-test assuming identical activity between two configurations are smaller than 0.001). Because the configuration of the drying chamber is the only difference among run 4, 5 and 6, the different observed $I_{\mathrm{p}}/I_{\mathrm{f}}$ can be explained by the different flow patterns in these configurations. The significantly longer median T_{res} for the drying particles in configuration A, combined with most of the drying gas streamlines that circulate back to the nozzle, suggest that particles following those streamlines could be repeatedly subjected to high gradients of velocity, humidity, temperature, pressure and species while circulating to the region of initial mixing between the droplet spray and drying gas; plus recirculation increases chances for inter-particle collisions and wall deposition (*15*). In comparison to configuration C, configuration B has a less uniform drying condition as observed from its multimodal T_{dry} distribution (see Figure 6b and Figure 6c). In addition, configuration B has a small region of closed recirculation streamlines near the drying gas entrance, which could potentially trap particles and increase their chances of collision. Indeed, after performing experimental run 5, significant particle accumulation was observed in the cylindrical plenum region, in which the closed recirculation zone was predicted by the CFD simulations. Particle collisions can be enhanced in this flow recirculation region, possibly creating a comminution zone, as particles are trapped in circular trajectories and increase the energy state on their surfaces. This process promotes more efficient particle size reduction and surface modification(*16*, *17*).

3.2. $I_{\mathrm{p}}/I_{\mathrm{f}}$ as a function of atomization droplet size and surfactant

We systematically investigated the impact of atomization droplet size and surfactant in the formulation in the fluorescence intensity of reconstituted GFP. In particular, in the absence of the surfactant polysorbate 20, the atomization droplet size has a significant influence on the fluorescence intensity of reconstituted GFP. From runs 1-3, the $I_{\mathrm{p}}/I_{\mathrm{f}}$ increased from 0.58 to 0.86 while the atomizing droplets increased in Dv50 from 11.2 μm to 24.7 μm (Figure 7). It is worth noting the Sauter mean diameter (SMD) of the droplets increased from 6.9 μm to 18.4 μm, suggesting a 2.6 times increase in surface area per volume of aerosolized solution.

In the presence of polysorbate 20, however, the $I_{\mathrm{p}}/I_{\mathrm{f}}$ are independent of the aerosol droplet sizes. From run 6-9, $I_{\mathrm{p}}/I_{\mathrm{f}}$ stays constant between 0.93-0.96, while the aerosol Dv50 more than doubled from 7.5 μm to 16.6 μm.

Our results demonstrated the sensitivity of GFP on interface-induced damages and the protective effect of polysorbate 20 on such damages, in agreement with earlier findings on other proteins. Protein and peptides are known to denature at liquid-gas interfaces (*18*). Surfactant like polysorbate 20 is a common ingredient in pharmaceutical formulations that can preferentially migrate to the interface and protect protein molecule from interface-induced damages. In spray drying, with the addition of increasing surface active molecules in the feedstock, proteins can eventually disappear from the surface of spray-dried particles (*19*).

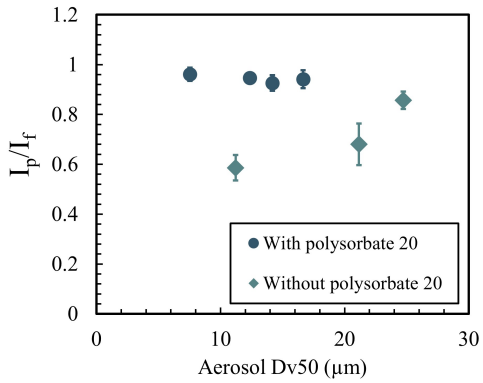

Figure 7. I_p/I_f of GFP as a function of Dv50 of the atomizing droplets with or without the use of polysorbate 20. The experiments with polysorbate 20 are run 6-9 and the experiments without polysorbate 20 are run 1-3.

4. Summary

In this study we demonstrated that using green fluorescent protein as a model biologic provides an efficient and sensitive method for investigating the thermophysical and chemical stresses induced on the material during dehydration of a bioformulation in our a new room-temperature aerosol drying process. We have shown that only a small concentration of GFP (≤ 0.03 mg/ml) is needed to generate robust fluorescence intensity measurements that can reflect the structural integrity of GFP. The fluorescence intensity can provide evaluation of GFP quality within just a few minutes of offline measurement of light spectra emitted from the reconstituted powder sample in comparison to hours of chromatography analysis for non-fluorescent proteins. The fluorophore, enclosed in a beta-barrel scaffold (*5*), of GFP was found to be sensitive to interfacial phenomena and recirculating flow patterns in the drying chamber. We showed that the interfacial and mechanical stresses can cause irreversible change to the fluorescence intensity of GFP during dehydration process, making the damage easily detectable by fluorescence measurements.

The findings of this work suggest the importance of optimizing flow patterns in the design of scaled-up drying processes. Significantly longer particle residence time and flow recirculation in large dryers could subject sensitive dehydrated material to additional thermophysical and chemical stresses caused by gradients of velocity, temperature, pressure, chemical species and humidity in the drying chamber. In addition, we demonstrated that small closed recirculation regions, like the ones near the drying gas inlet, can trap the dehydrated particles and increase the chances for additional, collision-related, damage of the protein structure.

5. Acknowledgement

This work was supported by the National Science Foundation under STTR Phase I Grant award #2304461. The authors acknowledge the use of Princeton's Imaging and Analysis Center, which is partially supported by the Princeton Center for Complex Materials, a National Science Foundation MRSEC program (DMR-2011750). The numerical simulations presented in this article were performed on computational resources managed and supported by Princeton Research Computing of the Office of the Dean for Research of Princeton University. We express our gratitude to Professor Robert K. Prud'homme at the Department of Chemical and Biological Engineering of Princeton University for helpful discussions and providing access to the equipment in his laboratory.

References

(1) Mezhericher, M.; Nunes, J.K.; Guzowski, J.J.; Stone, H.A. Aerosol-assisted synthesis of submicron particles at room temperature using ultra-fine liquid atomization, *Chemical Engineering Journal* **2018**, *346*, 606–620.

(2) Mezhericher, M.; Razorenov, N.; Mazor, G.; Ju, Y.; Stone, H.A. Submicron aerosols of liquid fuels: Method of production, experimental characterization and a semi-empirical model, *Applied Energy* **2019**, *235*, 1651–1663.

(3) Poozesh, S.; Mezhericher, M.; Pan, Z.; Chaudhary, U.; Manikwar, P.; Stone, H.A. Rapid Room-Temperature Aerosol Dehydration Versus Spray Drying: A Novel Paradigm in Biopharmaceutical Drying Technologies, *Journal of Pharmaceutical Sciences* **2024**, *113* (4), 974–981.

(4) Butreddy, A.; Janga, K.Y.; Ajjarapu, S.; Sarabu, S.; Dudhipala, N. Instability of therapeutic proteins—An overview of stresses, stabilization mechanisms and analytical techniques involved in Lyophilized proteins, *International Journal of Biological Macromolecules* **2021**, *167*, 309–325.

(5) Stepanenko, O.V.; Stepanenko, O.V.; Kuznetsova, I.M.; Verkhusha, V.V.; Turoverov, K.K. Beta-barrel scaffold of fluorescent proteins: folding, stability and role in chromophore formation, *International Review of Cell and Molecular Biology* **2013**, *302*, 221–278.

(6) Fukuda, H.; Arai, M.; Kuwajima, K. Folding of green fluorescent protein and the cycle3 mutant, *Biochemistry* **2000**, *39* (39), 12025–12032.

(7) Hsu, S.T.D.; Blaser, G.; Behrens, C.; Cabrita, L.D.; Dobson, C.M.; Jackson, S.E. Folding Study of Venus Reveals a Strong Ion Dependence of Its Yellow Fluorescence under Mildly Acidic Conditions 2, *Journal of Biological Chemistry* **2010**, *285* (7), 4859–4869.

(8) Rehman, N.; Ullah, H.; Alam, S.; Jan, A.K.; Khan, S.; Tariq, M. Surface and thermodynamic study of micellization of non ionic surfactant/diblock copolymer system as revealed by surface tension and conductivity, *J. Mater. Environ. Sci* **2017**, *8* (4), 1161–1167.

(9) Mezhericher, M.; Stone, H.A. Possible, impossible, and expected diameters and production rates of droplets in aerosols and sprays, *Physical Review Fluids* **2022**, *7* (6), 063602.

(10) Stuart, A.; Ord, K. *Kendall's Advanced Theory of Statistics, Distribution Theory*; John Wiley & Sons, 2010; Vol. 1.

(11) Mezhericher, M.; Levy, A.; Borde, I. Three-dimensional spray-drying model based on comprehensive formulation of drying kinetics, *Drying Technology* **2012**, *30* (11-12), 1256–1273.

(12) Mezhericher, M.; Levy, A.; Borde, I. Multi-scale multiphase modeling of transport phenomena in spray-drying processes, *Drying Technology* **2015**, *33* (1), 2–23.

(13) Mezhericher, M.; Levy, A.; Borde, I. Theoretical drying model of single droplets containing insoluble or dissolved solids, *Drying Technology* **2007**, *25* (6), 1025–1032.

(14) Azad, R.S. Turbulent flow in a conical diffuser: A review, *Experimental Thermal and Fluid Science* **1996**, *13* (4), 318–337.
(15) Mezhericher, M.; Levy, A.; Borde, I. Probabilistic hard-sphere model of binary particle–particle interactions in multiphase flow of spray dryers, *International Journal of Multiphase Flow* **2012**, *43*, 22–38.
(16) Bnà, S.; Ponzini, R.; Cestari, M.; Cavazzoni, C.; Cottini, C.; Benassi, A. Investigation of particle dynamics and classification mechanism in a spiral jet mill through computational fluid dynamics and discrete element methods, *Powder Technology* **2020**, *364*, 746–773.
(17) Muehlenfeld, C.; Kann, B.; Windbergs, M.; Thommes, M. Solid dispersions prepared by continuous cogrinding in an air jet mill, *Journal of Pharmaceutical Sciences* **2013**, *102* (11), 4132–4139.
(18) Koepf, E.; Eisele, S.; Schroeder, R.; Brezesinski, G.; Friess, W. Notorious but not understood: how liquid-air interfacial stress triggers protein aggregation, *International Journal of Pharmaceutics* **2018**, *537* (1-2), 202–212.
(19) Adler, M.; Unger, M.; Lee, G. Surface composition of spray-dried particles of bovine serum albumin/trehalose/surfactant, *Pharmaceutical Research* **2000**, *17*, 863–870.

Appendix A. Computational setup

In our Computational Fluid Dynamic model, the droplets were modeled as multi-component evaporating spherical particles. A total of 500 DPM droplet injections were generated based on the Rosin-Rammler distribution, with diameters ranging from 0.5 µm to 30 µm. The particles were injected at 22°C from a small ring located at the exit of the atomization nozzle, forming a cone with a cone angle of 13 degrees. For the discrete phase model (DPM), the particle status was set to be 'trapped' when particles made contact with the wall, and 'escaped' when collected by the filter.

Appendix B. Study of the independence of numerical solution on the mesh size

A polyhedral mesh was used for the computational domain, with boundary layer mesh cells grown from the walls to ensure a no-slip boundary condition. Adaptive mesh refinement was employed in regions downstream of the drying gas and atomizing gas inlets, where the velocity magnitude gradients were high, to capture the flow features with greater accuracy. A grid independence study was performed to ensure the accuracy of the numerical simulations. Five sets of computational grids were investigated, with total mesh cell counts of 0.70 million (M1), 1.33 million (M2), 2.51 million (M3), 3.97 million (M4), and 5.81 million (M5). We compared the change in azimuthally averaged z-velocity along the chamber radius at a cross section of z = 0.1 m for all five grids in Figure B1. As the number of mesh cells increased, the averaged z-velocity converged at all locations along the radius. The difference in velocity at the center between M4 and M5 was less than 2%, indicating good convergence. Therefore, the computational grid M4 was adopted for all simulations in this study.

The criteria for a converged solution were defined as residuals reaching 10^{-3} for continuity, momentum, k, and ϵ, and 10^{-6} for energy and species. Typically, convergence was achieved after 1000 numerical iterations. The computations were performed on clusters of Princeton Research Computing. A typical simulation took approximately 5 hours, utilizing 16 parallel 2.6 GHz Intel Skylake CPU cores.

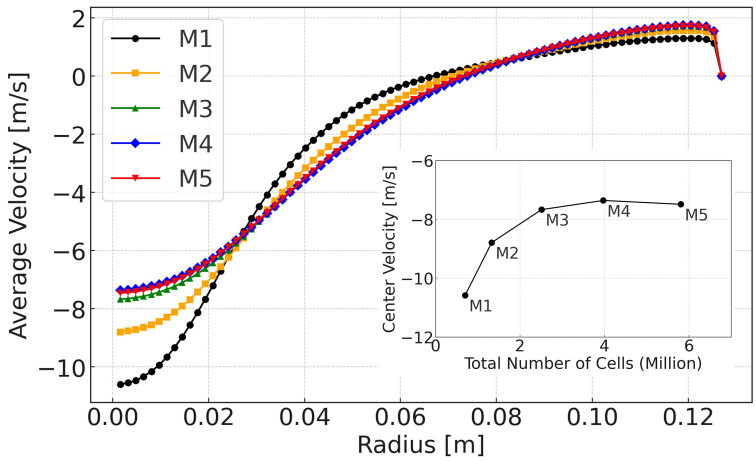

Figure B1. Study of numerical solution dependence on mesh size. Change in azimuthally averaged z-velocity along the chamber radius at a cross section of z = 0.1 m for numerical grids M1, M2, M3, M4, and M5. The change of z-velocity with the total number of cells is also presented.